Check for updates

Vanadium ferrite-doped mesoporous bioactive glass-ceramics: controlled cisplatin delivery in chemohyperthermia

Sajjad Omidian,[a] Masoumeh Haghbin Nazarpak, [ID] *[b] Zohreh Bagher*[cd] and Fathollah Moztarzadeh[a]

This study explores the multifunctional application of vanadium ferrite-doped mesoporous bioactive glass-ceramics (MBGCs), presenting a novel approach to synergistically integrate chemohyperthermia and controlled cisplatin delivery in cancer treatment. Using the sol–gel method, MBGC formulations were developed, which VF0510 (a formulation containing 5 mol% V_2O_5 and 10 mol% Fe_2O_3) identified as the optimal composition due to its superior magnetic properties, bioactivity, and controlled drug delivery capabilities. The previously established mesoporous architecture of VF0510, validated in our earlier study, enabled effective cisplatin loading and sustained release in this work. Calorimetric analyses revealed that VF0510 achieved a controlled therapeutic temperature of 41.5 °C under an alternating magnetic field, meeting the optimal range for hyperthermia-based treatments. Drug loading studies demonstrated that hydroxypropyl cellulose (HPC)-coated VF0510 provided a sustained release of 68% over 48 hours, significantly reducing the burst effect while maintaining prolonged therapeutic action. *In vitro* assays using MG63 osteosarcoma cells demonstrated statistically significant results ($P < 0.01$), with cisplatin-loaded VF0510 reducing cell viability by 45% within 48 hours through apoptosis induction, as confirmed by flow cytometry. This dual-modality platform integrates localized magnetic hyperthermia with controlled chemotherapy delivery, addressing challenges such as systemic toxicity and drug resistance. The results highlight the critical role of vanadium ferrite in enhancing magnetic response and bioactivity, while the HPC coating ensures sustained and efficient drug release. Future research should optimize the thermoresponsive properties of polymer coatings and validate findings through *in vivo* models, paving the way for safer, more effective cancer therapies combining hyperthermia and chemotherapy.

1 Introduction

According to recent statistics from the World Health Organization, cancer accounts for approximately 10 million deaths annually, highlighting the urgent need for innovative therapeutic strategies to enhance efficacy while reducing adverse effects. One promising approach combines magnetic hyperthermia with targeted drug delivery systems.[1–3]

Magnetic hyperthermia utilizes alternating current (AC) magnetic fields to generate localized heat within magnetic nanoparticles, selectively raising tumor temperatures to 40–43 °C, a range that induces cancer cell apoptosis while sparing healthy tissues.[1,4] The heating mechanism primarily involves Néel relaxation (realignment of magnetic moments) and Brownian motion (physical rotation of particles), both of which contribute to thermal energy dissipation.[1,2,4,5] This localized heating enhances cell membrane permeability, facilitating increased uptake of chemotherapeutic agents and producing a synergistic effect when combined with drug delivery.[6] Uniform thermal distribution is essential for optimizing therapeutic efficacy and minimizing probable damage to healthy tissues, necessitating precise control over nanoparticle concentration, distribution, and applied AC magnetic field parameters.[7]

Chemohyperthermia, which combines chemotherapy with hyperthermia, has emerged as a highly effective strategy in cancer treatment, enhancing the cytotoxic effects of drugs such as cisplatin by increasing tumor cell membrane permeability and disrupting cellular repair mechanisms.[8,9] In clinical practice, chemohyperthermia has demonstrated significant success in the treatment of non-muscle-invasive bladder cancer (NMIBC), leading to reduced recurrence rates and improved patient outcomes.[10,11] Despite its effectiveness, systemic toxicity and drug resistance remain major challenges in cisplatin

[a]*Biomaterials Group, Faculty of Biomedical Engineering (Center of Excellence), Amirkabir University of Technology (Tehran Polytechnic), Tehran, Iran*

[b]*New Technologies Research Center (NTRC), Amirkabir University of Technology (Tehran Polytechnic), Tehran, Iran. E-mail: haghbin@aut.ac.ir*

[c]*ENT and Head and Neck Research Center and Department, the Five Senses Health Institute, School of Medicine, Iran University of Medical Sciences, Tehran, Iran*

[d]*Department of Tissue Engineering & Regenerative Medicine, Faculty of Advanced Technologies in Medicine, Iran University of Medical Sciences, Tehran, Iran. E-mail: Bagher.z@iums.ac.ir*

therapy, necessitating innovative delivery systems that ensure targeted release while minimizing side effects.

Cisplatin, a platinum-based chemotherapeutic agent, remains the cornerstone in treating various cancers, including high-grade osteosarcoma.[12,13] However, its clinical use is limited by challenges such as systemic toxicity and the development of drug resistance.[14–18] Encapsulation of cisplatin within mesoporous bioactive glass-ceramics (MBGCs) provides a targeted delivery approach, reducing systemic exposure while ensuring higher drug concentrations at tumor sites.[19] The combination of MBGCs with magnetic hyperthermia presents a dual-modality approach that leverages the benefits of localized heating and sustained drug release to enhance therapeutic efficacy.

Bioactive glass-ceramics have gained considerable attention in biomedical research due to their biocompatibility, bioactivity, and tunable physicochemical properties, making them ideal candidates for cancer therapy applications.[20–23] Recent advancements have focused on doping magnetic components such as vanadium ferrite (VF) to enhance magnetic properties, making them suitable for hyperthermia applications while enabling high drug loading capacity and controlled release.[24–27] The combination of bioactive glass-ceramics and vanadium ferrite enhances their heating efficiency under an AC magnetic field, providing an effective solution for localized hyperthermia and drug delivery.

Moreover, incorporating thermosensitive polymer coatings such as hydroxypropyl cellulose (HPC) onto MBGCs can further refine drug release profiles, minimizing the initial burst effect and enabling a sustained release over time.[28] Such coatings enhance physical and chemical interactions between the drug and the porous structure of the glass-ceramic matrix, ensuring better drug retention and controlled diffusion.[29] This approach provides a more predictable drug release pattern, crucial for effective cancer therapy.[30]

Previous research has demonstrated the bioactivity and magnetic properties of MBGCs;[24] however, challenges remain in achieving uniform heating and sustained drug release, both of which are crucial for clinical applications.[31] Magnetic hyperthermia combined with targeted cisplatin delivery represents a promising strategy for improving cancer treatment by overcoming drug resistance, minimizing systemic toxicity, and enhancing therapeutic precision. While magnetic nanoparticles have shown significant potential in hyperthermia applications, limitations such as non-uniform heating and uncontrolled drug diffusion hinder their clinical translation.[32,33] The incorporation of vanadium ferrite into MBGCs addresses these challenges by enhancing magnetic responsiveness, improving drug encapsulation, and enabling controlled release.

Building upon our previous findings on the bioactivity of VF-doped glass-ceramics,[24] this study further evaluates the multifunctional properties of the optimized VF0510 composition, which refers to a sample doped with 5 mol% vanadium oxide (V_2O_5) and 10 mol% iron oxide (Fe_2O_3). We systematically investigate its magnetic heating efficiency, heat generation capacity, and drug delivery performance. Additionally, we assess its cytotoxic and apoptosis-inducing effects in MG63 osteosarcoma cells to determine its suitability for combined

hyperthermia and chemotherapy applications. Our results provide a comprehensive assessment of VF0510's potential for cancer treatment and contribute to bridging the gap between preclinical research and clinical translation. Future research should focus on optimizing synthesis parameters, evaluating long-term material stability, and conducting *in vivo* studies to validate its clinical applicability.

2 Materials and method

2.1. Synthesis and thermal stabilization of MBGCs

MBGC powders were prepared by first synthesizing bioactive glass *via* a sol–gel process, followed by controlled thermal treatment to induce partial crystallization and convert the amorphous glass into a glass-ceramic structure.[24] The formulation consisted of 60 mol% total oxides (SiO_2, V_2O_5, and Fe_2O_3), 36 mol% CaO, and 4 mol% P_2O_5.

The following high-purity precursors were used in the synthesis process:

• Tetramethyl orthosilicate (TMOS, Sigma-Aldrich, >99%) as silicon source,

• Triethyl phosphate (TEP, Sigma-Aldrich, >99%) as phosphorus source,

• Calcium nitrate tetrahydrate ($Ca(NO_3)_2 \cdot 4H_2O$, Merck, >99%) as calcium source,

• Iron(III) nitrate nonahydrate ($Fe(NO_3)_3 \cdot 9H_2O$, Sigma-Aldrich, >98%),

• Vanadyl sulfate hydrate ($VOSO_4 \cdot xH_2O$, Sigma-Aldrich, >97%),

• Deionized water, and

• Nitric acid (HNO_3, Sigma-Aldrich, 70%, 1.5 M solution).

All materials were handled under controlled conditions to ensure homogeneity. The resulting sol was aged at 37 °C for 7 days to allow polycondensation and gel formation. The gel, along with its supernatant containing soluble by-products, was retained to preserve compositional integrity. Drying was carried out sequentially at 70 °C for 24 hours and 140 °C for 48 hours. Final thermal stabilization was performed by heating the dried gel to 800 °C at a rate of 5 °C min^{-1}, holding at this temperature for 2 hours to induce crystallization, and then allowing it to cool gradually under ambient conditions. The final MBGC powders were classified into five groups, with compositions detailed in Table 1.

2.2. Differential scanning calorimetry (DSC

To determine the appropriate temperature and heating profile for the thermal stabilization of MBGC powders, differential

Table 1 Chemical composition of MBGC samples (mole%)

Sample	VF00	VF0505	VF1010	VF1005	VF0510
CaO	36	36	36	36	36
P_2O_5	4	4	4	4	4
SiO_2	60	50	40	45	45
V_2O_5	0	5	10	10	5
Fe_2O_3	0	5	10	5	10

scanning calorimetry (DSC) was performed on the VF00 sample using a Netzsch STA 409 PC/PG instrument. Approximately 150 mg of powder was heated from room temperature to 1250 °C at a rate of 5 °C min^{-1} under an air atmosphere.

2.3. Magnetic property analysis

The magnetic properties of MBGC samples were characterized using Vibrating Sample Magnetometry (VSM; Lake Shore Model 7404) at room temperature, with a magnetic field range of −10,000 to 10 000 Oe.

2.4. Calorimetric testing

Heat generation efficiency was assessed by dispersing MBGC samples (VF0505, VF1010, VF1005, VF0510) in 10 ml of distilled water with polyvinyl alcohol (PVA) as a stabilizer. The suspension was exposed to an alternating magnetic field (0–50 mT at 300 kHz), and temperature changes were monitored using an infrared sensor.

2.5. Density measurement

The bulk density of the MBGC powder was determined using the Archimedes principle in deionized water as the immersion medium. Approximately 1.0 g of each powder was compacted into a pellet using uniaxial pressing and sintered at 800 °C to obtain consolidated samples. The dry weight (W_d), suspended weight (W_s), and wet weight (W_w) were recorded, and the density was calculated using the equation eqn (1):

$$\rho = \frac{W_d}{W_w - W_s} \times \rho_{water} \qquad (1)$$

where ρ_{water} is the density of water at 25 °C (0.997 g cm^{-3}). All measurements were repeated in triplicate, and mean values are reported.

2.6. Core–shell structure and polymer coating

2.6.1 Surface modification of MBGC. Surface modification was performed using 3-methacryloxypropyltrimethoxysilane (MPTS) as a coupling agent. The glass-ceramic powder (25 g) was mixed with 2.5 g MPTS, 250 ml solvent, and 0.15 g para-methoxyphenol, stirred for 30 minutes, and cured at 90 °C to achieve effective surface modification.

2.6.2 Polymer binding to MBGC. Hydroxypropyl cellulose (HPC, 5% w/v) was oxidized with sodium periodate to introduce aldehyde groups, enhancing covalent binding to the modified glass-ceramic surface. The polymer was combined with the glass-ceramic particles and stirred for 12 hours, followed by washing three times with deionized water, each for 10 minutes.

2.7. Fourier transform infrared spectroscopy (FTIR)

FTIR analysis (Bomem MB 100 spectrometer) was conducted using KBr pelletization. The spectra were recorded in the 400–4000 cm^{-1} range at a scan speed of 23 scans per minute with a resolution of 4 cm^{-1}.

2.8. Drug loading and release analysis

2.8.1 Drug loading. Cisplatin was loaded into the MBGC core–shell structure by dissolving 2 mg of cisplatin in 10 ml of deionized water and adding it to 10 mg of MBGC powder. The mixture was stirred at 45 °C for 3 hours, followed by 24-hours stabilization at room temperature. The loaded samples were washed and dried under controlled conditions.

2.8.2 Drug release. Drug release studies were conducted by immersing samples in PBS at 37 °C and 43 °C. Sampling was performed at predetermined intervals, and cisplatin concentrations were quantified using UV-vis spectroscopy at 263 nm (UV-Vis Spectrophotometer, Analytikjena, SPECORD 210, Germany). Drug release kinetics were analyzed using mathematical models (zero-order, first-order, Higuchi, Korsmeyer-Peppas) to identify the dominant release mechanism.

2.9. Cytotoxicity evaluation

Cytotoxicity was assessed using an MTT assay with MG63 osteosarcoma cells, which were obtained from the National Cell Bank of Iran (NCBI). A 0.5 mg ml^{-1} MTT solution in PBS was added to each well and incubated at 37 °C for 4 hours. Formazan crystals were dissolved in 100 μL of DMSO, and absorbance was recorded at 570 nm. Cell viability was calculated using eqn (2)

$$\text{Percentage of viable cells} = (A/B) \times 100, \qquad (2)$$

where, A = viable cells in the experimental well and B = viable cells in the control well. Tissue culture plastic (TCP) served as the control. The evaluation was performed in triplicate to ensure data reliability.

2.10. Evaluation of apoptotic and necrotic cells

Apoptotic and necrotic cell death was evaluated using Annexin V-FITC/Propidium Iodide (PI) staining. MG63 cells were seeded in 6-well plates and treated with MBG, MBG-Cis, and MBG-Cis-HPC formulations. After 24 hours of incubation, cells were harvested, stained with Annexin V-FITC and PI, and analyzed using flow cytometry (BD FACSCalibur, BD Biosciences, USA). A minimum of 10 000 events were recorded per sample, and cell populations were categorized into live, early apoptotic, late apoptotic, and necrotic cells.

2.11. Statistical study

Quantitative data presented as mean ± standard deviation (SD). Statistical significance was determined using one-way ANOVA followed by Tukey's post-hoc test, with a significance threshold set at $P < 0.05$.

3 Results and discussion

3.1. Thermal behavior and crystallization onset of MBGC powders

The DSC curve of the VF00 sample (Fig. 1) revealed two distinct endothermic events. The first, occurring between ~250–350 °C, is attributed to the removal of physically adsorbed water,
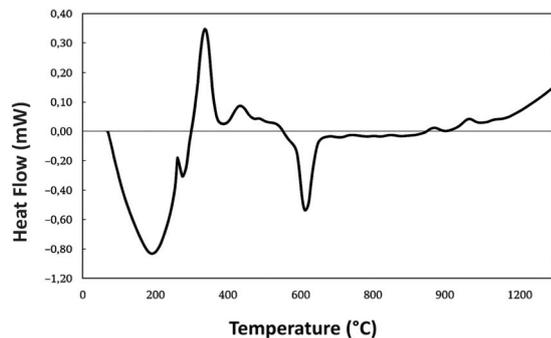
Fig. 1 Differential scanning calorimetry (DSC) curve of the VF00 sample.

alcohols from polycondensation, and residual surfactants. The second endothermic peak, observed around 450 °C, corresponds to the condensation of silanol groups and the decomposition of nitrate species. A gradual rise in the thermal signal from 800 °C to 950 °C indicated the onset of crystallization, suggesting a suitable heat-treatment temperature near 800 °C for controlled conversion into glass-ceramic. These findings support the thermal behavior and processing stability of the synthesized glass, although full thermal degradation analysis would require complementary tests. The absence of sharp or multiple exothermic peaks supports the structural homogeneity of the glass matrix, confirming that no phase-separated domains were present prior to calcination.[34,35]

3.2. Magnetic properties of the bioactive glass-ceramics

The magnetic properties of MBGCs were analyzed *via* VSM at room temperature. Hysteresis loops (Fig. 2) and key parameters—remanent magnetization (M_r), coercivity (Hc), and saturation magnetization (M_s)—(Table 2) elucidate their hyperthermia potential.

As the concentration of magnetic dopants (vanadium and iron oxides) increased in the glass-ceramic matrix, the area enclosed by the hysteresis loop also increased, indicating enhanced energy dissipation—an essential property for efficient magnetic hyperthermia. The VF1010 sample exhibited the
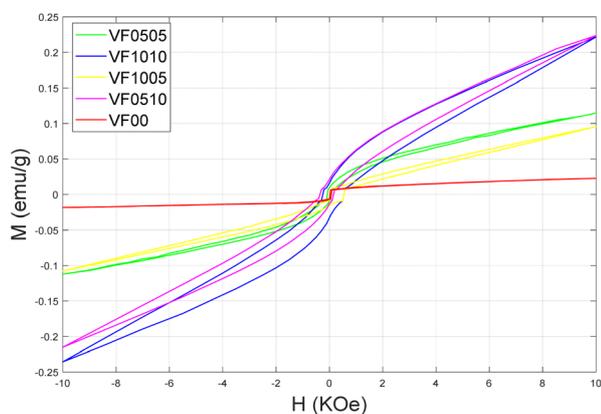

Fig. 2 Hysteresis loops of magnetic bioactive glass-ceramic samples measured at room temperature.

largest hysteresis loop area due to its high iron oxide content, aligning with prior findings.[36–38] The control sample (VF00) showed the weakest response, while VF0505 demonstrated a 15-fold increase in hysteresis area, and VF1010 achieved a 100-fold increase, marking it as the most magnetically responsive sample. VF0510, although less active than VF1010, ranked second.

The addition of 5% vanadium and iron oxides variably enhanced the hysteresis loop area. For instance, 5% vanadium oxide in VF1005 increased the area by 40% compared to VF0505, while 5% iron oxide in VF0510 caused a fourfold increase to 366.44 erg g^{-1}. These results emphasize the stronger influence of iron oxide over vanadium oxide in improving magnetic properties, crucial for high-performance applications.

3.3. Thermal properties of bioactive glass-ceramics

Ferrimagnetic and ferromagnetic materials generate heat when exposed to an alternating magnetic field, essential for hyperthermia applications. The heat generation capacity of MBGCs (VF0505, VF1005, VF0510, and VF1010) was evaluated using the power loss formula:[39]

$$P_{FM} = \mu_0 f \int H \, dm \qquad (3)$$

where, P_{FM} represents the total heat generated per unit volume, μ_0 is the permeability of the vacuum, f is the frequency, H is the magnetic field strength, and M is the magnetization. Heat generation depends on frequency and hysteresis loop area. The specific absorption rate (SAR) estimates heat production per unit volume.[40,41]

Vibrating sample magnetometry (VSM) results revealed the significant impact of iron and vanadium doping on heat generation. Samples exhibited temperature increases of approximately 15 °C (VF0505), 22 °C (VF1005), 68 °C (VF0510), and 83 °C (VF1010) after 720 seconds in an alternating magnetic field. Notably, VF1010 and VF0510 reached the therapeutic range of 41–43 °C, ideal for hyperthermia-based cancer treatments.

Comparative analysis showed that 5% vanadium oxide in VF1005 caused a modest 7 °C rise, while 5% iron oxide in VF0510 resulted in a significant 53 °C increase. Combining vanadium and iron oxides in VF1010 produced a synergistic temperature increase of 68 °C, emphasizing iron oxide's dominant role in heat generation. Optimizing iron oxide content is thus critical for desirable magnetic and thermal properties. Calorimetric tests showed temperature increases of 11 °C (VF0505), 23 °C (VF1005), 41.5 °C (VF0510), and 51.5 °C (VF1010). These experimental values, lower than theoretical predictions, reflect non-ideal experimental conditions.[42–44] Despite discrepancies, VF1010 and VF0510 demonstrated rapid, controlled temperature rises suitable for hyperthermia.

The findings underscore that iron oxide alone has a stronger effect on heat generation than vanadium oxide, but their combination exhibits a synergistic effect, significantly enhancing the heating capabilities of bioactive glass-ceramics for targeted thermal therapy in cancer treatment.

Table 2 Magnetic properties of bioactive glass-ceramics

Sample code	Remanence magnetization M_r (emu g^{-1})	Coercivity Hc (Oe)	Saturation magnetization M_s (emu g^{-1})	Interpolated hysteresis area (erg g^{-1})
VF00	0.0065	25	0.0227	5.47
VF0505	0.0087	75	0.1147	74.16
VF1010	0.0155	250	0.2216	524.53
VF1005	0.0090	50	0.0955	103.26
VF0510	0.0207	350	0.2236	366.44

Fig. 3 depicts the heat generation profiles of glass-ceramic samples under an alternating magnetic field, showing a non-linear temperature rise due to heat dissipation. Samples VF1010 and VF0510 demonstrated the highest heat production, maintaining controlled therapeutic heating without exceeding safe thresholds, highlighting their clinical potential. Further research should optimize thermal stability under continuous magnetic exposure and assess performance in biological environments. Integrating these materials into multifunctional chemohyperthermia platforms could advance targeted and effective cancer therapies.

The XRD patterns of all prepared MBGC formulations were comprehensively reported in our previous study.[24] Key diffraction peaks identified corresponded to wollastonite ($CaSiO_3$ (w)), hydroxyapatite (H), and coulsonite (FeV_2O_4 (C)), with the specific crystalline phases varying according to the Fe and V dopant ratios. These crystalline signatures confirmed partial crystallization of the glass matrix following thermal treatment and aligned with the materials' bioactivity and magnetic functionality. For brevity, only the XRD pattern of the optimized VF0510 sample is shown in Fig. 4(a), and readers are referred to our prior publication for full comparative XRD profiles.

Similarly, scanning electron microscopy (SEM) was previously used to analyze the surface morphology and microstructure of all MBGC compositions.[24] Here, we present the SEM image of VF0510 as a representative sample (Fig. 4(b)). The
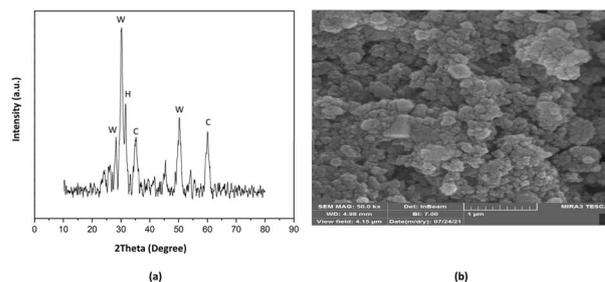
Fig. 4 (a) X-ray diffraction (XRD) pattern of the VF0510 sample; (b) SEM micrograph of VF0510 powder.

observed microstructure reveals aggregated, irregularly shaped particles in the submicron range. These features are consistent with the material's mesoporous structure and partially crystalline nature, as also supported by XRD and BET analyses.[24]

The Archimedes method was employed to estimate the bulk density of the thermally stabilized MBGC samples. Among the synthesized compositions, the VF0510 sample—selected as the optimal formulation—exhibited a bulk density of 2.74 ± 0.03 g cm^{-3}, consistent with the incorporation of high atomic weight dopants (Fe_2O_3 and V_2O_5) into the silicate network. This value aligns well with previous reports for Fe- and V-doped sol–gel-derived bioactive glass-ceramics, which typically show bulk densities in the range of 2.6–3.1 g cm^{-3}.[45–47] The relatively high density further supports the formation of partially crystalline phases (*e.g.*, wollastonite and coulsonite), as corroborated by XRD analysis. This enhanced density is indicative of effective network densification during thermal treatment and may contribute to the mechanical integrity and bioactivity of the final material.

3.4. FTIR analysis for surface modification

Fourier-transform infrared (FTIR) spectroscopy was performed on VF0510 sample to confirm the silanization process. Comparative FTIR spectra of unmodified and silane-modified VF0510 samples (Fig. 5) revealed successful introduction of silane chain on surface functional groups.

Surface modification of bioactive glass-ceramic with a silane coupling agent significantly altered FTIR spectra. Prior to silanization, bands corresponding to silanol groups (Si–OH) were observed at 3200–3600 cm^{-1} (O–H stretching) and 900–1000 cm^{-1} (Si–OH bending); also a broad band at ~1640 cm^{-1} region was attributed to O–H bending vibrations. Post-modification, the asymmetric stretching band of Si–O–Si at
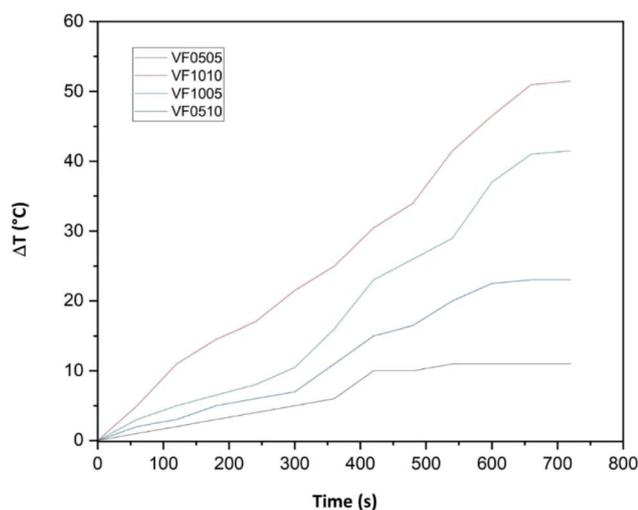
Fig. 3 Calorimetric test results for magnetic bioactive glass-ceramic samples VF0505, VF1010, VF1005, and VF0510.
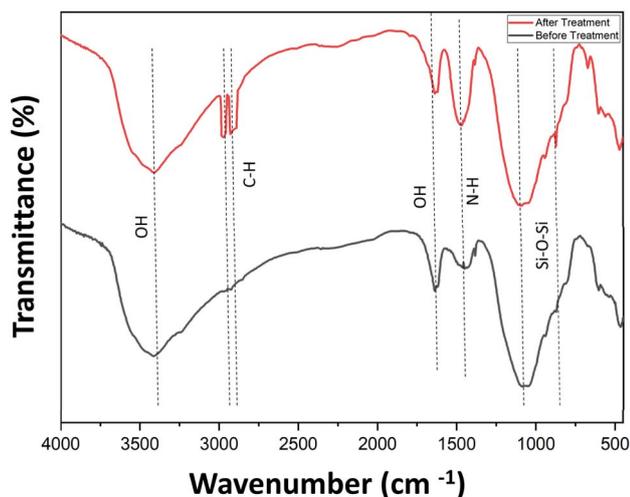
Fig. 5 FTIR spectra of the VF0510 sample: before silanization and after silanization.

$1000–1200\ cm^{-1}$ intensified, with a bending band at $\sim 800\ cm^{-1}$ confirming siloxane bond formation. Enhanced bands at $1460\ cm^{-1}$ indicated amine groups from the silane agent, while stretching bands at $2800–3000\ cm^{-1}$ signified alkyl groups from the propyl silane chain. These spectral changes confirm successful silanization of the bioactive glass-ceramic particles. While FTIR identifies functional groups introduced by the silane agent, further studies are required to comprehensively assess substrate interactions and binding mechanisms. These results establish a foundation for exploring the modified glass-ceramics' functional and structural properties in advanced applications.[48,49]

3.5. Drug release studies

3.5.1 Calibration and quantification of cisplatin release. Cisplatin release from MBG-Cis and MBG-Cis-HPC formulations was analyzed using UV-Vis spectrophotometry. Standard solutions, prepared in a 1 : 1 water-DMSO mixture with serial dilutions, identified cisplatin's maximum absorption at 263 nm, enabling quantification of its release from both formulations. Cisplatin encapsulation was confirmed, and drug release studies were conducted. At intervals, supernatants were analyzed *via* UV-vis. Absorbance values plotted using the Beer–Lambert law generated a calibration curve, confirming high quantification sensitivity ($R^2 = 0.9956$). This ensured reliable and precise drug quantification throughout the study.[50]

3.5.2 Comparison of drug loading efficiency and release kinetics of MBG-Cis before and after hydroxypropyl cellulose (HPC) coating. The difference in drug loading efficiency between MBG-Cis and MBG-Cis-HPC is attributed to their design and surface properties. In MBG-Cis, cisplatin is loaded into mesopores without a coating agent, leading to partial drug loss and a lower loading efficiency of 64%. Conversely, MBG-Cis-HPC includes a hydroxypropyl cellulose (HPC) coating, which stabilizes surface properties, reduces initial burst release, and enhances physical and chemical interactions with the drug,

achieving a higher loading efficiency of 79%. This coating improves drug retention and stability, making MBG-Cis-HPC more suitable for controlled drug delivery.

Cisplatin release from MBG-Cis and MBG-Cis-HPC was studied at intervals up to 240 hours in phosphate-buffered saline (PBS); in which samples heated to 43 °C for 720 seconds.[51,52] The release behavior indicated that an increase in temperature of magnetic nanoparticles up to 43 °C correlated with enhanced cisplatin release, suggesting a temperature-dependent mechanism.[53] Also, a semi-permeable cellulose acetate membrane (12–14 kDa) prevented nanoparticle migration. The release profiles for both formulations are shown in Fig. 6.

The MBG-Cis formulation, with cisplatin loaded into mesopores, exhibited a faster release rate due to its high surface area and porosity. In contrast, MBG-Cis-HPC demonstrated controlled, sustained release. The HPC coating acts as a diffusion barrier, reducing initial burst release and providing gradual drug release over time. Its hydrophilic nature causes swelling upon water contact, restricting cisplatin diffusion.[30]

Drug release in MBG-Cis is governed by diffusion through the mesopores, while MBG-Cis-HPC follows a dual release mechanism involving both the mesopores and polymer matrix. These results in lower cumulative release for MBG-Cis-HPC compared to MBG-Cis. Although HPC's thermosensitive properties were expected to cause a higher burst release, none was observed, potentially due to its need for longer exposure or higher temperatures for full release.[30] The HPC coating forms a gel-like barrier under heat, slowing release and creating a complex diffusion path. Strong interactions between the drug and polymer could further delay cisplatin release, even at elevated temperatures.[54] Experimental conditions like temperature control and exposure time may also influence release profiles, causing deviations.[55,56]

These findings highlight MBG-Cis as a fast-release carrier, while MBG-Cis-HPC offers controlled, sustained release, making it ideal for cancer therapies requiring precise drug
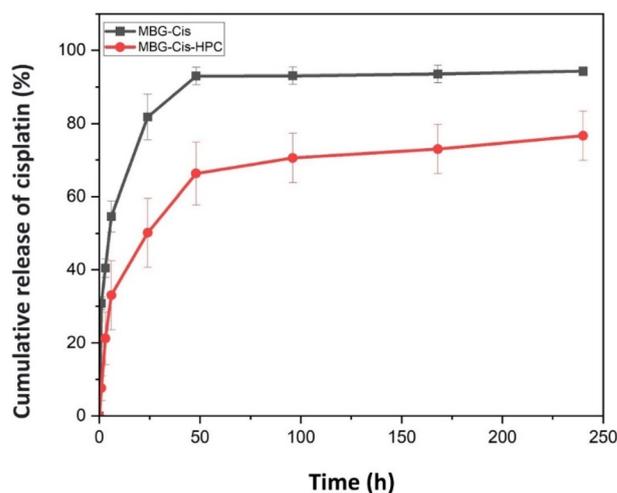

Fig. 6 Cisplatin release profiles from MBG-Cis and MBG-Cis-HPC at 1, 3, 6, 24, 48, 96, 148, and 240 hours.

Table 3 Analysis of drug release models for the MBG-Cis structure based on equations and R^2 values

Release model	Model equation	R^2 value	Release mechanism analysis
Zero-order	$y = 0.2728x + 46.846$	0.4623	Lower fit with experimental data
First-order	$y = -0.0108x + 3.7191$	0.6311	Moderate fit
Higuchi	$y = 5.245x + 32.407$	0.7047	Best fit with experimental data
Korsmeyer-Peppas	$y = 0.4831x + 2.3946$	0.498	Lower fit with experimental data

dosing. Further optimization of polymer coatings could improve thermoresponsive behavior and refine drug release kinetics for clinical applications in drug delivery and hyperthermia-assisted treatments.

3.5.2.1 Analysis of drug release models for the MBG-Cis structure. Table 3 analyzes drug release models for MBG-Cis, focusing on coefficient of determination (R^2) values. The Higuchi model, with an R^2 of 0.7047, showed the best fit, indicating that drug release is primarily governed by diffusion within the porous matrix. In contrast, zero-order, Korsmeyer-Peppas, and first-order models demonstrated lower correlations. The Higuchi model, commonly applied to porous solid matrices, confirms that MBG-Cis's mesoporous architecture facilitates controlled, diffusion-driven release. While the first-order model partly represents sustained release, it does not adequately capture the overall behavior. These findings underscore MBG-Cis's potential for controlled drug release in advanced therapeutic applications.

Fig. 7(a–d) show the linear fitting plots for the zero-order, first-order, Higuchi, and Korsmeyer-Peppas models, respectively, based on the drug release data for the MBG-Cis sample. Among these, the Higuchi model (Fig. 5(c)) exhibited the highest R^2 value (0.7047), indicating diffusion-controlled drug release through the mesoporous matrix as the dominant

mechanism. The visual fitting corroborates the quantitative analysis summarized in Table 3.

3.5.2.2 Analysis of drug release models for the MBG-Cis-HPC structure. Table 4 compares drug release models for MBG-Cis-HPC. The first-order model ($R^2 = 0.9676$) showed the best fit, indicating controlled, exponential release. The Higuchi model ($R^2 = 0.8655$) also correlated well, highlighting diffusion as a significant mechanism. Zero-order and Korsmeyer-Peppas models exhibited lower R^2 values, indicating lesser relevance. The first-order model underscores the MBG-Cis-HPC structure's ability to minimize burst release and achieve sustained, controlled drug release, making it suitable for targeted therapeutic applications. This release profile enhances drug efficacy by providing consistent, long-term delivery.[57,58]

Fig. 8(a–d) presents the linear fitting plots for the zero-order, first-order, Higuchi, and Korsmeyer-Peppas models, respectively, based on the drug release data for the MBG-Cis-HPC formulation. Among these models, the first-order model (Fig. 8(b)) yielded the highest coefficient of determination ($R^2 = 0.9676$), indicating that the release follows a concentration-dependent mechanism, characteristic of systems where drug diffusion occurs from a matrix with a polymeric barrier. These visual findings are consistent with the quantitative data summarized in Table 4.
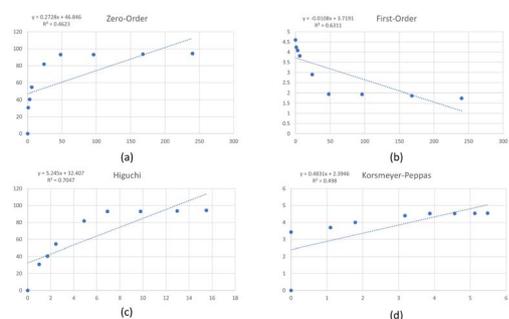

Fig. 7 Linear fitting of MBG-Cis drug release data based on: (a) Zero-order model, (b) First-order model, (c) Higuchi model, (d) Korsmeyer-Peppas model.
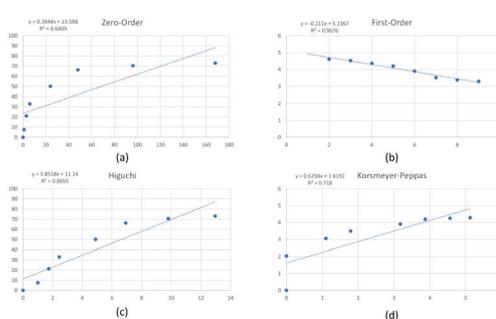

Fig. 8 Linear fitting of MBG-Cis-HPC drug release data based on: (a) Zero-order model, (b) First-order model, (c) Higuchi model, (d) Korsmeyer-Peppas model.

Table 4 Analysis of drug release models for the MBG-Cis-HPC structure based on equations and R^2 values

Release model	Model equation	R^2 value	Release mechanism analysis
Zero-order	$y = 0.3848x + 23.588$	0.6409	Lower fit with experimental data
First-order	$y = -0.211x + 5.1367$	0.9676	Best fit with experimental data
Higuchi	$y = 5.8518x + 11.14$	0.8655	Relatively high fit
Korsmeyer-Peppas	$y = 0.6258x + 1.6192$	0.718	Lower fit with experimental data

Table 5 Comparison of drug loading efficiency and release models for MBG–Cis and MBG–Cis–HPC structures

Structure	Loading efficiency (%)	Best-fit model	R^2 value	Primary release mechanism
MBG–Cis–HPC	79	First-order	0.97	Controlled diffusion through pores and HPC coating
MBG–Cis	64	Higuchi	0.71	Diffusion through the solid porous matrix

The MBG-Cis-HPC system demonstrated a promising controlled and sustained release platform. Two cisplatin-loaded magnetic bioactive glass-ceramic structures were studied, with drug release governed by diffusion through mesoporous architecture. MBG-Cis-HPC showed a superior first-order fit ($R^2 = 0.97$), ensuring minimal burst release and sustained exponential release. Conversely, MBG-Cis aligned better with the Higuchi model ($R^2 = 0.71$), indicating diffusion-dominated release through the porous matrix.

The hydroxypropyl cellulose (HPC) coating in MBG-Cis-HPC enhances release control, reduces initial burst release, improves sustained release, and optimizes the system for prolonged therapeutic applications by regulating drug diffusion (Table 5).

A representative image of the VF0510 glass-ceramic sample at different stages—before drug loading, after cisplatin incorporation, and following HPC coating—is provided in Fig. 9. This visual confirmation supports the preparation pathway and distinguishes the appearance of each functionalized formulation.

3.6. Cytotoxicity evaluation of drug-loaded structure

VF0510 was selected for cytotoxicity evaluation based on its optimal physicochemical properties. The formulations tested included:

(1) Magnetic bioactive glass-ceramic (MBG),

(2) Cisplatin-loaded glass-ceramic (MBG-Cis),

(3) Cisplatin-loaded, hydroxypropyl cellulose-coated glass-ceramic (MBG-Cis-HPC).

MG63 osteosarcoma cells were cultured on these samples, with tissue culture plastic (TCP) serving as the control.

Fig. 10 presents MG63 cell viability for MBG, MBG-Cis, and MBG-Cis-HPC, highlighting a statistically significant reduction in MBG-Cis compared to the other groups ($P < 0.01$). Table 6 quantifies the percentage of viable cells at 24, 48, and 72 hours.

MBG and MBG-Cis-HPC maintained high cell viability above 75% at 72 hours, demonstrating favorable biocompatibility. In contrast, MBG-Cis exhibited a sharp decline in viability,
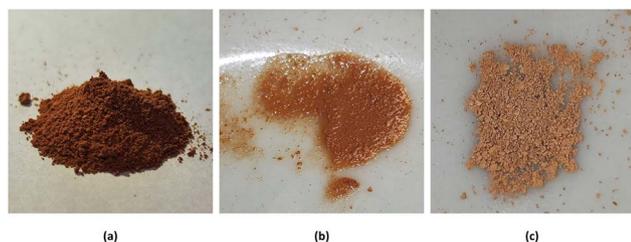

Fig. 10 Cell viability of MG63 cells cultured on the base VF0510 sample (MBG), drug-loaded sample (MBG-Cis), drug-loaded sample with hydroxypropyl cellulose coating (MBG-Cis-HPC), and tissue culture plastic (TCP) as the control; all showing a statistically significant difference with a P-value of less than 0.01 compared to TCP.

reaching 25.46% at 72 hours, indicating significant cytotoxicity due to rapid cisplatin release ($P < 0.01$ *vs.* MBG and MBG-Cis-HPC). The presence of the HPC coating in MBG-Cis-HPC mitigated this effect, leading to a higher viability of 77.78% at 72 hours through sustained drug release ($P < 0.05$ *vs.* MBG-Cis). These findings highlight the critical role of polymer coatings in regulating drug release, reducing burst toxicity, and enhancing biocompatibility. The HPC layer acted as a diffusion barrier, effectively preventing excessive initial drug exposure while maintaining therapeutic efficacy over the time.[7,59–63]

The controlled release of cisplatin in MBG-Cis-HPC reduces its toxicity toward healthy cells, making it a promising candidate for localized chemotherapy. However, further dose-response studies and *in vivo* evaluations are required to confirm its potential for biomedical applications. Future research should focus on optimizing polymer coatings to refine release kinetics and enhance therapeutic precision. Additionally, further biocompatibility assays, such as live/dead staining and apoptosis detection, are necessary to provide a more comprehensive assessment of the material's safety. Long-term stability studies and *in vivo* efficacy evaluations in tumor models will be crucial for validating its potential for clinical translation.

Fig. 9 Representative images of the VF0510 sample: (a) as-prepared glass-ceramic powder, (b) after cisplatin loading (MBG-Cis), and (c) after hydroxypropyl cellulose (HPC) coating (MBG-Cis-HPC).
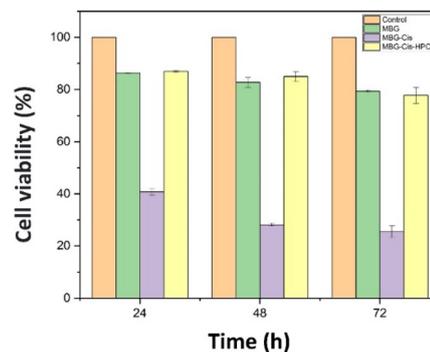
Table 6 Cell viability (%) of samples after 24, 48, and 72 hours in the MTT assay ($n = 3$)

Sample code	Cell viability (%) after 24 hours	Cell viability (%) after 48 hours	Cell viability (%) after 72 hours
MBG	86.37 ± 0.34	82.69 ± 1.86	79.34 ± 0.43
MBG-Cis	40.72 ± 1.29	28.15 ± 0.57	25.46 ± 2.16
MBG-Cis-HPC	86.92 ± 0.41	84.91 ± 1.83	77.78 ± 2.96

3.7. Evaluation of apoptotic and necrotic cells *via* Annexin V-FITC/PI staining

The evaluation of apoptotic and necrotic cells using Annexin V-FITC/PI staining is illustrated in Fig. 11(a–e). Fig. 11(a) shows the control sample (TCP), which exhibited the highest cell viability, serving as a benchmark for biocompatibility.

Fig. 11(b) emphasizes the high biocompatibility of the MBG sample, showing relatively elevated cell viability compared to the control. While MBG supports cell viability, it lacks anti-cancer benefits without a therapeutic agent like cisplatin. Fig. 11(c) demonstrates the MBG-Cis sample's high early and late apoptosis levels, indicating enhanced anticancer activity due to the synergy between MBG's magnetic properties and cisplatin's efficacy.[64] These properties enable targeted cisplatin delivery, reducing systemic toxicity.[14–16] Optimizing drug release is essential to minimize risks from uncontrolled cisplatin release.[17,18,65]

Fig. 11(d) shows the MBG-Cis-HPC sample achieving a sustained cisplatin release, resulting in balanced apoptosis and necrosis induction. The hydroxypropyl cellulose (HPC) coating regulates release, reduces toxicity, and enhances cisplatin stability and bioavailability. Fig. 11(e) reveals the high cytotoxicity of released cisplatin, with substantial late apoptosis and minimal viable cells. Although effective in inducing apoptosis, uncontrolled release poses risks like nephrotoxicity and neurotoxicity, highlighting the need for controlled mechanisms.[18,66] Table 7 summarizes apoptosis, necrosis, and live cell proportions for all samples.

The TCP control group showed the highest percentage of live cells, confirming minimal cytotoxicity. The MBG sample demonstrated a 27% reduction in viable cells compared to the control, maintaining good biocompatibility. The MBG-Cis sample exhibited a 45% reduction in viability due to cisplatin's cytotoxicity; while the MBG-Cis-HPC formulation maintained ~12% higher viability, emphasizing the role of HPC in reducing cisplatin-induced toxicity.[30] The Released Cis sample had the lowest cell viability (97.5% reduction), reflecting the adverse effects of uncontrolled cisplatin release. However, the MBG-Cis-HPC system's controlled release resulted in higher viability compared to MBG-Cis, supporting the benefits of thermosensitive HPC coatings in balancing toxicity and efficacy.[67–69] The MBG-Cis-HPC sample exhibited the highest necrosis, possibly due to delayed cisplatin release, although the necrosis was lower than apoptosis (39.5%) and live cells (47.8%). MBG showed moderate necrosis due to its magnetic components and partial vanadium and iron release.[52,70,71] The MBG-Cis sample exhibited lower necrosis than the control, highlighting cisplatin's ability to induce apoptosis without significant necrosis. Released Cis showed minimal necrosis but high late apoptosis, confirming cisplatin's potent anticancer effects and underscoring the risks of uncontrolled release.[72,73]

The MBG-Cis-HPC sample demonstrated increased necrosis and late apoptosis but moderate early apoptosis, suggesting the polymer coating influences release kinetics and cell death modes. Promoting apoptosis over necrosis minimizes inflammation, improving clinical outcomes.[74,75] Released Cis exhibited 97.8% total apoptosis, confirming its efficacy in inducing cancer cell death, followed by MBG-Cis with 57%, further validating cisplatin's apoptotic potential.

Flow cytometry results revealed that the MBG-Cis sample exhibited significantly elevated levels of early apoptosis (37.5%) compared to late apoptosis (19.5%), indicating rapid induction of programmed cell death due to cisplatin release. Conversely, the MBG-Cis-HPC sample showed a more balanced apoptotic response, with early apoptosis at 14.7% and late apoptosis at 24.8%, reflecting controlled cisplatin release facilitated by the hydroxypropyl cellulose (HPC) coating. These differences highlight the polymer coating's critical role in modulating drug release kinetics and its therapeutic efficacy.

Temperature significantly impacts drug release kinetics and cell behavior. Elevated temperatures enhance drug diffusion from bioactive glass-ceramics, leading to faster, less controlled release, especially in thermosensitive polymer systems. Thermal exposure can also alter cell surface protein functionality, impacting cell–material interactions.[76,77] While this study did not directly investigate temperature's effects on drug release and cell response, it remains critical for future research to
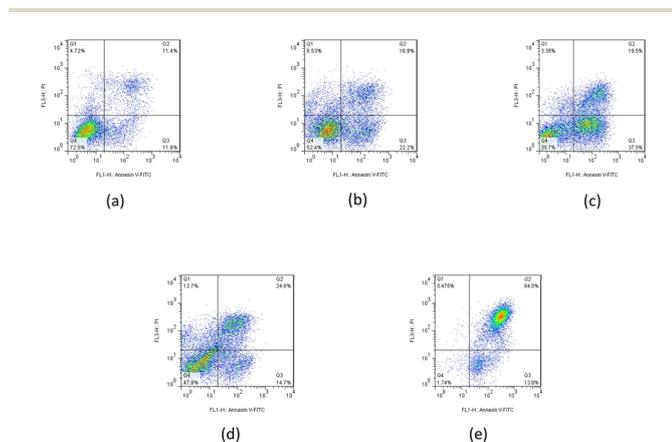

Fig. 11 Flow cytometry analysis of MG63 cells treated with (a) TCP, (b) MBG, (c) MBG-Cis, (d) MBG-Cis-HPC and (e) released Cis for 24 hours.

Table 7 Summary of apoptotic and necrotic cell evaluation *via* Annexin V-FITC/PI staining

Sample code	Q1 (necrosis)	Q2 (late apoptosis)	Q3 (early apoptosis)	Q4 (live cells)
MBG	8.53	16.9	22.2	52.4
MBG-Cis	3.35	19.5	37.5	39.7
MBG-Cis-HPC	12.7	24.8	14.7	47.8
Released Cis	0.475	84.0	13.8	1.74
TCP	4.72	11.4	11.9	72.0

optimize the system for biomedical applications.[78] These findings underline the importance of integrating controlled release mechanisms to maximize therapeutic efficacy while minimizing systemic toxicity.

4 Conclusions

This study builds upon our previously synthesized mesoporous bioactive glass-ceramics (MBGCs) doped with vanadium and iron, focusing on their application in controlled cisplatin delivery and magnetic hyperthermia. Among the formulations, VF0510 (a formulation containing 5 mol% V_2O_5 and 10 mol% Fe_2O_3) exhibited optimal magnetic heating efficiency, bioactivity, and drug delivery properties. Building on our previously confirmed mesoporous architecture, the present study demonstrated effective cisplatin loading and controlled release behavior of the VF0510 formulation. The incorporation of a hydroxypropyl cellulose (HPC) coating significantly reduced the initial burst effect, ensuring sustained drug release (68% over 48 hours) while minimizing systemic toxicity.

Calorimetric analysis demonstrated VF0510's ability to maintain a stable temperature range of 41–43 °C, making it suitable for hyperthermia applications. Cytotoxicity studies on MG63 osteosarcoma cells indicated a 45% reduction in viability within 48 hours, while the HPC-coated formulation improved biocompatibility by mitigating localized toxicity and sustaining therapeutic action. These results underscore the potential of the VF0510-HPC system in enhancing drug efficacy and reducing side effects.

The integration of magnetic hyperthermia with controlled drug delivery presents a promising approach for targeted cancer therapy. Future research should focus on optimizing thermoresponsive polymer coatings, conducting *in vivo* evaluations, and exploring synergistic effects with complementary treatments such as immunotherapy and photothermal therapy.

Data availability

The data supporting the findings of this study are available from the corresponding author upon reasonable request.

Author contributions

Sajjad Omidian: conceptualization, resources, investigation, formal analysis, visualization, writing – original draft. Masoumeh Haghbin Nazarpak: conceptualization, funding acquisition, resources, validation, writing – review and editing. Zohreh Bagher: resources, writing – review & editing. Fathollah Moztarzadeh (deceased): project administration, supervision. The authors wish to honor the memory of Professor Fathollah Moztarzadeh and acknowledge his invaluable contributions to this work. His guidance and expertise were crucial to the success of this project.

Conflicts of interest

There are no conflicts to declare.

Acknowledgements

References

1 P. IP Soares, I. MM Ferreira, R. AGBN Igreja, C. MM Novo and J. PMR Borges, Application of hyperthermia for cancer treatment: recent patents review, *Recent Pat. Anti-Cancer Drug Discovery*, 2012, **7**(1), 64–73.

2 R. L. Souhami, I. Tannock, P. Hohenberger and J.-C. Horiot, *Oxford Textbook of Oncology*, Oxford Univ. Press, 2002.

3 B. Rezaei, S. Mostufa, E. Azizi, Y. A. Wang, C. Li, J. Gómez-Pastora, *et al.*, Investigation on the Magnetic Hyperthermia Performance of Commercial Iron Oxide Magnetic Nanoparticles, *IEEE Trans. Magn.*, 2025, DOI: **10.1109/TMAG.2025.3535358**.

4 K. Wu, D. Su, J. Liu, R. Saha and J.-P. Wang, Magnetic nanoparticles in nanomedicine: a review of recent advances, *Nanotechnology*, 2019, **30**(50), 502003.

5 T. K. Jain, J. Richey, M. Strand, D. L. Leslie-Pelecky, C. A. Flask and V. Labhasetwar, Magnetic nanoparticles with dual functional properties: drug delivery and magnetic resonance imaging, *Biomaterials*, 2008, **29**(29), 4012–4021.

6 C. C. Berry, Progress in functionalization of magnetic nanoparticles for applications in biomedicine, *Recent Pat. Anti-Cancer Drug Discovery*, 2009, **42**(22), 224003.

7 A. Yadollahpour, S. A. Hosseini and A. Yadollahpour, Magnetic nanoparticle based hyperthermia: a review of the physiochemical properties and synthesis methods, *Int. J. Pharm. Res. Allied Sci.*, 2016, **5**(2), 242–246.

8 R. D. Issels, L. H. Lindner, J. Verweij, P. Wust, P. Reichardt, B.-C. Schem, *et al.*, Neo-adjuvant chemotherapy alone or with regional hyperthermia for localised high-risk soft-tissue sarcoma: a randomised phase 3 multicentre study, *Lancet Oncol.*, 2010, **11**(6), 561–570.

9 A. A. Luderer, N. F. Borrelli, J. N. Panzarino, G. R. Mansfield, D. M. Hess, J. L. Brown, *et al.*, Glass-ceramic-mediated, magnetic-field-induced localized hyperthermia: response of a murine mammary carcinoma, *Radiat. Res.*, 1983, **94**(1), 190–198.

10 E. I. Liem, H. Crezee, J. J. de la Rosette and T. M. de Reijke, Chemohyperthermia in non-muscle-invasive bladder cancer:

An overview of the literature and recommendations, *Int. J. Hyperthermia*, 2016, **32**(4), 363–373.

11 N. Zeng, M.-Y. Xu, J.-X. Sun, C.-Q. Liu, J.-Z. Xu, Y. An, *et al.*, Hyperthermia intravesical chemotherapy acts as a promising alternative to bacillus Calmette–Guérin instillation in non-muscle-invasive bladder cancer: a network meta-analysis, *Front. Oncol.*, 2023, **13**, 1164932.

12 J. Gu, S. Su, Y. Li, Q. He, J. Zhong and J. Shi, Surface modification– complexation strategy for cisplatin loading in mesoporous nanoparticles, *J. Phys. Chem. Lett.*, 2010, **1**(24), 3446–3450.

13 J.-Y. Huang, M.-H. Chen, W.-T. Kuo, Y.-J. Sun and F.-H. Lin, The characterization and evaluation of cisplatin-loaded magnetite–hydroxyapatite nanoparticles (mHAp/CDDP) as dual treatment of hyperthermia and chemotherapy for lung cancer therapy, *Ceram. Int.*, 2015, **41**(2), 2399–2410.

14 A. J. Wagstaff, S. D. Brown, M. R. Holden, G. E. Craig, J. A. Plumb, R. E. Brown, *et al.*, Cisplatin drug delivery using gold-coated iron oxide nanoparticles for enhanced tumour targeting with external magnetic fields, *Inorg. Chim. Acta*, 2012, **393**, 328–333.

15 Y. Zhong, C. Jia, X. Zhang, X. Liao, B. Yang, Y. Cong, *et al.*, Targeting drug delivery system for platinum(ɪᴠ)-Based antitumor complexes, *Eur. J. Med. Chem.*, 2020, **194**, 112229.

16 E. Voulgari, A. Bakandritsos, S. Galtsidis, V. Zoumpourlis, B. P. Burke, G. S. Clemente, *et al.*, Synthesis, characterization and *in vivo* evaluation of a magnetic cisplatin delivery nanosystem based on PMAA-graft-PEG copolymers, *J. Controlled Release*, 2016, **243**, 342–356.

17 M. Pourmadadi, M. M. Eshaghi, E. Rahmani, N. Ajalli, S. Bakhshi, H. Mirkhaef, *et al.*, Cisplatin-loaded nanoformulations for cancer therapy: a comprehensive review, *J. Drug Delivery Sci. Technol.*, 2022, **77**, 103928.

18 A. Callejo, L. Sedó-Cabezón, I. Domenech Juan and J. Llorens, Cisplatin-induced ototoxicity: effects, mechanisms and protection strategies, *Toxics*, 2015, **3**(3), 268–293.

19 M. Babincova, V. Altanerova, C. Bergemann and P. Babinec, *In vitro* analysis of cisplatin functionalized magnetic nanoparticles in combined cancer chemotherapy and electromagnetic hyperthermia, *IEEE Trans. NanoBiosci.*, 2008, **7**(1), 15–19.

20 M. Miola, Y. Pakzad, S. Banijamali, S. Kargozar, C. Vitale-Brovarone, A. Yazdanpanah, *et al.*, Glass-ceramics for cancer treatment: so close, or yet so far?, *Acta Biomater.*, 2019, **83**, 55–70.

21 W. Holand and G. H. Beall, *Glass-ceramic Technology*, John Wiley & Sons, 2019.

22 S. Kargozar, F. Baino, S. Hamzehlou, R. G. Hill and M. Mozafari, Bioactive glasses entering the mainstream, *Drug discovery today*, 2018, **23**(10), 1700–1704.

23 C. Wu, W. Fan, Y. Zhu, M. Gelinsky, J. Chang, G. Cuniberti, *et al.*, Multifunctional magnetic mesoporous bioactive glass scaffolds with a hierarchical pore structure, *Acta Biomater.*, 2011, **7**(10), 3563–3572.

24 S. Omidian, M. H. Nazarpak, Z. Bagher and F. Moztarzadeh, The effect of vanadium ferrite doping on the bioactivity of mesoporous bioactive glass-ceramics, *RSC Adv.*, 2022, **12**(39), 25639–25653.

25 D. Cong, Z. Zhang, M. Xu, J. Wang, X. Pu, Z. Huang, *et al.*, Vanadium-Doped Mesoporous Bioactive Glass Promotes Osteogenic Differentiation of rBMSCs *via* the WNT/β-Catenin Signaling Pathway, *ACS Appl. Bio Mater.*, 2023, **6**(9), 3863–3874.

26 N. Hamrouni, H. Oudadesse, B. Lefeuvre, O. Merdrignac-Conanec and M. Ben-Attia, Exploring the impact of vanadium on physical, structural and thermal properties of bioactive glass 46S6: a comparative study with other metallic elements, *J. Therm. Anal. Calorim.*, 2023, **148**(23), 13245–13261.

27 A. M. Deliormanlı, S. Oguzlar and K. Ertekin, Photoluminescence and decay characteristics of cerium, gallium and vanadium-containing borate-based bioactive glass powders for bioimaging applications, *Ceram. Int.*, 2021, **47**(3), 3797–3807.

28 M. Bagheri, S. Shateri, H. Niknejad and A. A. Entezami, Thermosensitive biotinylated hydroxypropyl cellulose-based polymer micelles as a nano-carrier for cancer-targeted drug delivery, *J. Polym. Res.*, 2014, **21**, 1–15.

29 L. Dai and C. Si, Recent advances on cellulose-based nano-drug delivery systems: design of prodrugs and nanoparticles, *Curr. Med. Chem.*, 2019, **26**(14), 2410–2429.

30 D. E. Ciolacu, R. Nicu and F. Ciolacu, Cellulose-based hydrogels as sustained drug-delivery systems, *Materials*, 2020, **13**(22), 5270.

31 S. V. Spirou, M. Basini, A. Lascialfari, C. Sangregorio and C. Innocenti, Magnetic hyperthermia and radiation therapy: radiobiological principles and current practice, *Nanomaterials*, 2018, **8**(6), 401.

32 A. G. A. Abdelhamid, *Magnetic Field Responsive Nano-Platforms Composed of Magnetic Nanoparticle-Loaded Metal-Organic Frameworks for Anticancer Targeted Drug Delivery*, Université Paul Sabatier-Toulouse III, 2023.

33 R. Staruch, R. Chopra and K. Hynynen, Localised drug release using MRI-controlled focused ultrasound hyperthermia, *Int. J. Hyperthermia*, 2011, **27**(2), 156–171.

34 V. Saraswat, S. K. Pal, N. Mehta, A. Kumar and M. Imran, Thermal analysis of novel third-generation phase-change materials with zinc as a chemical modifier, *RSC Adv.*, 2023, **13**(6), 3602–3611.

35 D. Janovszky, M. Sveda, A. Sycheva, F. Kristaly, F. Zámborszky, T. Koziel, *et al.*, Amorphous alloys and differential scanning calorimetry (DSC), *J. Therm. Anal. Calorim.*, 2022, 1–17.

36 N. A. Spaldin, *Magnetic Materials: Fundamentals and Applications*, Cambridge university press, 2010.

37 F. Fiorillo, C. Appino, M. Pasquale and G. Bertotti. Hysteresis in magnetic materials, *The Science of Hysteresis*, 2006, vol. 3, pp. 1–190.

38 K. M. Krishnan, *Fundamentals and Applications of Magnetic Materials*, Oxford University Press, 2016.

39 Q. A. Pankhurst, J. Connolly, S. K. Jones and J. Dobson, Applications of magnetic nanoparticles in biomedicine, *Recent Pat. Anti-Cancer Drug Discovery*, 2003, **36**(13), R167.

40 S. Huang, S. Wang, A. Gupta, D. Borca-Tasciuc and S. Salon, On the measurement technique for specific absorption rate of nanoparticles in an alternating electromagnetic field, *Meas. Sci. Technol.*, 2012, **23**(3), 035701.

41 E. Garaio, J. M. Collantes, J. A. Garcia, F. Plazaola, S. Mornet, F. Couillaud and O. Sandre, A wide-frequency range AC magnetometer to measure the specific absorption rate in nanoparticles for magnetic hyperthermia, *J. Magn. Magn. Mater.*, 2014, **368**, 432–437.

42 I. Andreu and E. Natividad, Accuracy of available methods for quantifying the heat power generation of nanoparticles for magnetic hyperthermia, *Int. J. Hyperthermia*, 2013, **29**(8), 739–751.

43 H. Gavilán, S. K. Avugadda, T. Fernández-Cabada, N. Soni, M. Cassani, B. T. Mai, *et al.*, Magnetic nanoparticles and clusters for magnetic hyperthermia: optimizing their heat performance and developing combinatorial therapies to tackle cancer, *Chem. Soc. Rev.*, 2021, **50**(20), 11614–11667.

44 H. Ghayour, M. Abdellahi, N. Ozada, S. Jabbrzare and A. Khandan, Hyperthermia application of zinc doped nickel ferrite nanoparticles, *J. Phys. Chem. Solids*, 2017, **111**, 464–472.

45 E. Ilik, E. Kavaz, G. Kilic, S. A. Issa, G. ALMisned and H. Tekin, Synthesis and characterization of vanadium(v) oxide reinforced calcium-borate glasses: experimental assessments on $Al_2O_3/BaO_2/ZnO$ contributions, *J. Non-Cryst. Solids*, 2022, **580**, 121397.

46 H. Elsayed, A. Rincón Romero, G. Molino, C. Vitale Brovarone and E. Bernardo, Bioactive glass-ceramic foam scaffolds from 'inorganic gel casting'and sinter-crystallization, *Materials*, 2018, **11**(3), 349.

47 M. Elbadawi, Z. J. Wally and I. M. Reaney, Porous hydroxyapatite-bioactive glass hybrid scaffolds fabricated *via* ceramic honeycomb extrusion, *J. Am. Ceram. Soc.*, 2018, **101**(8), 3541–3556.

48 T. O. Rifane, K. E. M. Cordeiro, F. A. Silvestre, M. T. Souza, E. D. Zanotto, V. G. Araújo-Neto, *et al.*, Impact of silanization of different bioactive glasses in simplified adhesives on degree of conversion, dentin bonding and collagen remineralization, *Dent. Mater.*, 2023, **39**(2), 217–226.

49 S. Ferraris, A. Nommeots-Nomm, S. Spriano, E. Vernè and J. Massera, Surface reactivity and silanization ability of borosilicate and Mg-Sr-based bioactive glasses, *Appl. Surf. Sci.*, 2019, **475**, 43–55.

50 H. Motulsky and A. Christopoulos,*Fitting Models to Biological Data Using Linear and Nonlinear Regression: a Practical Guide to Curve Fitting*, Oxford University Press, 2004.

51 J. Shen and D. J. Burgess, *In vitro* dissolution testing strategies for nanoparticulate drug delivery systems: recent developments and challenges, *Drug Delivery Transl. Res.*, 2013, **3**, 409–415.

52 Z. Amini, S. S. Rudsary, S. S. Shahraeini, B. F. Dizaji, P. Goleij, A. Bakhtiari, *et al.*, Magnetic bioactive glasses/cisplatin loaded-chitosan (CS)-grafted-poly (ε-caprolactone) nanofibers against bone cancer treatment, *Carbohydr. Polym.*, 2021, **258**, 117680.

53 E. Kianfar, Magnetic nanoparticles in targeted drug delivery: a review, *J. Supercond. Novel Magn.*, 2021, **34**(7), 1709–1735.

54 C. Maderuelo, A. Zarzuelo and J. M. Lanao, Critical factors in the release of drugs from sustained release hydrophilic matrices, *Drug Delivery Transl. Res.*, 2011, **154**(1), 2–19.

55 S. Jamzad, L. Tutunji and R. Fassihi, Analysis of macromolecular changes and drug release from hydrophilic matrix systems, *Int. J. Pharm.*, 2005, **292**(1–2), 75–85.

56 H. Kim and R. Fassihi, Application of binary polymer system in drug release rate modulation. 2. Influence of formulation variables and hydrodynamic conditions on release kinetics, *J. Pharm. Sci.*, 1997, **86**(3), 323–328.

57 J. Siepmann and N. A. Peppas, Modeling of drug release from delivery systems based on hydroxypropyl methylcellulose (HPMC), *Adv. Drug Delivery Rev.*, 2012, **64**, 163–174.

58 A. Verma, K. Aljohani, B. S. Aljohani, B. Lal, Y. Jadeja, S. Ballal and M. Chahar, Innovations in cellulose-based hydrogels for enhanced wastewater treatment through adsorption, *Int. J. Biol. Macromol.*, 2025, 140660.

59 P. Carmona, *Structure evolution of phase-separated EC/HPC films for controlled drug release: Chalmers Tekniska Hogskola (Sweden)*, 2022.

60 S. Arabyazdi, M. Givarian, M. H. Nazarpak, A. Yazdanpanah and F. Moztarzadeh, Thermo-Responsive Doxorubicin Release from Bioactive Glass/Hydroxypropyl Cellulose Smart Core-Shell Nanoparticles for Bone Cancer Therapy, *J. Drug Delivery Sci. Technol.*, 2025, 107020.

61 S. Majumdar, Cellulose-based hydrogels for drug delivery applications, *Cellulose-Based Hydrogells*, Elsevier, 2025. pp. 259–279.

62 S. Parida and N. R. Kar, Exploring Magnetic Nanoparticles in Oncology: Synthesis to Therapeutic Application, *J. Bio-X Res.*, 2025, 0032.

63 A. S. Benjamin and S. Nayak, Iron oxide nanoparticles coated with bioactive materials: a viable theragnostic strategy to improve osteosarcoma treatment, *Discover Nano*, 2025, **20**(1), 1–22.

64 N. Gomez-Cerezo, D. Arcos and M. Vallet-Regí. Mesoporous bioactive glasses for biomedical composites, *Materials for Biomedical Engineering*, Elsevier, 2019. pp. 355–391.

65 Y. Xu, Y. Hu, P. Feng, W. Yang and C. Shuai, Drug loading/release and bioactivity research of a mesoporous bioactive glass/polymer scaffold, *Ceram. Int.*, 2019, **45**(14), 18003–18013.

66 G. O. Mwai, *Profiles and preventive strategies of nephrotoxicity among adult patients receiving cisplatin based regimens at Kenyatta national hospital*, 2014.

67 M. Yang, S. Y. H. Abdalkarim, H.-Y. Yu, R. A. Asad, D. Ge and Y. Zhou, Thermo-sensitive composite microspheres incorporating cellulose nanocrystals for regulated drug release kinetics, *Carbohydr. Polym.*, 2023, **301**, 120350.

68 C. Huang, H. Yu, Y. Gao, Y. Chen, S. Y. H. Abdalkarim and K. C. Tam, Recent Advances in Green and Efficient Cellulose Utilization Through Structure Deconstruction and Regeneration, *Adv. Funct. Mater.*, 2025, 2424591.

69 A. W. Alebachew, Y. Dong, S. Y. H. Abdalkarim, C. Wu and H.-Y. Yu, Recent progress of multifunctional nanocellulose-based pharmaceutical materials: a review, *Int. J. Biol. Macromol.*, 2025, 141427.

70 H. Bakhshi Aliabad, S. Khanamani Falahati-pour, H. Ahmadirad, M. Mohamadi, M. R. Hajizadeh and M. Mahmoodi, Vanadium complex: an appropriate candidate for killing hepatocellular carcinoma cancerous cells, *BioMetals*, 2018, **31**, 981–990.

71 Y. Oh, N. Lee, H. W. Kang and J. Oh, *In vitro* study on apoptotic cell death by effective magnetic hyperthermia with chitosan-coated $MnFe_2O_4$, *Nanotechnology*, 2016, **27**(11), 115101.

72 W. Lieberthal, V. Triaca and J. Levine, Mechanisms of death induced by cisplatin in proximal tubular epithelial cells: apoptosis *vs.* necrosis, *Am. J. Physiol.*, 1996, **270**(4), F700–F708.

73 H. Alborzinia, S. Can, P. Holenya, C. Scholl, E. Lederer, I. Kitanovic and S. Wölfl, Real-time monitoring of cisplatin-induced cell death, *PloS One*, 2011, **6**(5), e19714.

74 M. S. D'arcy, Cell death: a review of the major forms of apoptosis, necrosis and autophagy, *Cell Biol. Int.*, 2019, **43**(6), 582–592.

75 G. Yan, M. Elbadawi and T. Efferth, Multiple cell death modalities and their key features, *World Acad. Sci. J.*, 2020, **2**(2), 39–48.

76 K. Shafiee, S. Bazraei, A. Mashak and H. Mobedi, The Impact of Temperature on the Formation, Release Mechanism, and Degradation of PLGA-based *In Situ* Forming Implants, *J. Polym. Environ.*, 2024, 1–18.

77 Y. Zhao, H. Chen, J. Fu, A. Wang, X. Liu and X. Jiang, Drug-Loaded Microspheres on NIR-Responsive PLA/MXene Scaffolds: Controlled Release and Bone Tissue Regeneration, *ACS Appl. Bio Mater.*, 2025, **8**(1), 285–298.

78 E. T. Pashuck and M. M. Stevens, Designing regenerative biomaterial therapies for the clinic, *Sci. Transl. Med.*, 2012, **4**(160), 160sr4–sr4.